

## Article

# The Effect of Battery Configuration on Dendritic Growth: A Magnetic Resonance Microscopy Study on Symmetric Lithium Cells

Rok Peklar <sup>1,2</sup>, Urša Mikac <sup>1</sup> and Igor Serša <sup>1,3,\*</sup> 

<sup>1</sup> Jožef Stefan Institute, 1000 Ljubljana, Slovenia; rok.peklar@ijs.si (R.P.); ursa.mikac@ijs.si (U.M.)

<sup>2</sup> Jožef Stefan International Postgraduate School, 1000 Ljubljana, Slovenia

<sup>3</sup> Institute of Anatomy, Faculty of Medicine, University of Ljubljana, 1000 Ljubljana, Slovenia

\* Correspondence: igor.sersa@ijs.si; Tel.: +386-1-477-3696

**Abstract:** The potential of metallic lithium to become the anode material for next-generation batteries is hampered by significant challenges, chief among which is dendrite growth during battery charging. These dendritic structures not only impair battery performance but also pose safety risks. Among the non-destructive analytical techniques in battery research, Magnetic Resonance Imaging (MRI) stands out as a promising tool. However, the direct imaging of lithium by <sup>7</sup>Li MRI is limited by its low sensitivity and spatial resolution, making it a less effective way of imaging dendrite growth. Instead, a recently introduced indirect imaging approach which is based on <sup>1</sup>H MRI of the electrolyte was used in this study. This method was used to sequentially 3D image and thus monitor the charging process of lithium metal symmetric cells in three different electrical circuits, namely those composed of a single cell, four cells in parallel, and four cells in series. The measured sequential images allowed for the measurement of dendrite growth in each cell using volumetric analysis. The growth results confirmed the theoretical prediction that the growth across cells is uneven in a parallel circuit, and even in a series circuit. The methods presented in this study can also be applied to analyze many other dendrite-related issues in batteries.



**Citation:** Peklar, R.; Mikac, U.; Serša, I. The Effect of Battery Configuration on Dendritic Growth: A Magnetic Resonance Microscopy Study on Symmetric Lithium Cells. *Batteries* **2024**, *10*, 165. <https://doi.org/10.3390/batteries10050165>

Academic Editors: Chris Mi and Wei Gao

Received: 22 April 2024

Revised: 14 May 2024

Accepted: 15 May 2024

Published: 17 May 2024



**Copyright:** © 2024 by the authors. Licensee MDPI, Basel, Switzerland. This article is an open access article distributed under the terms and conditions of the Creative Commons Attribution (CC BY) license (<https://creativecommons.org/licenses/by/4.0/>).

## 1. Introduction

Lithium metal holds promise as an anode material for next-generation batteries due to its high specific capacity and low reduction potential, which could provide Lithium metal batteries with higher voltage and unprecedented energy densities. However, a significant challenge during the charging of these batteries is the formation of lithium dendrites, which can pierce the separator, posing the risk of short-circuiting and thermal runaway [1].

Lithium dendrite growth in lithium metal batteries can be primarily attributed to non-uniform lithium deposition on the anode surface during the charging process, as lithium ions are reduced and deposited as metallic lithium. Lithium dendrite growth is governed by electrochemomechanical forces that establish distinct behavior regimes, driven by chemical diffusion, electrodeposition, and deformation kinetics. The specific growth regime is initially determined by the applied current density but can evolve with the growth of deposits. At very low current densities, growth is thermodynamically suppressed, preventing dendrite formation. A base-controlled (mossy growth) regime is dominated by plastic flow due to electrodeposition stresses at lower current densities, whereas a tip-controlled (dendritic growth) regime is preferred at higher current densities, which is driven by electrolyte diffusion limitations. In many cases, dendritic growth occurs in the mixed regime, which is a result of both contributions [2,3]. As charging is ideally performed under relatively high currents, the tip-controlled regime dominates.

Here, lithium ions are consumed faster at the anode surface than they are replenished from the bulk electrolyte, leading to a localized drop in ion concentration. This drop increases the overpotential required for lithium deposition, promoting uneven lithium buildup and dendrite formation [4]. Strategies like using electrolytes with higher lithium salt concentrations, adding specific electrolyte additives, and designing advanced anode structures can mitigate the effects of concentration polarization and thus reduce dendrite growth [4–11].

In situ analytical techniques, such as NMR, MRI, and X-ray tomography, have become invaluable for the advancement of battery research. These techniques provide crucial insights into the dynamics of dendritic growth, offering the potential to guide the development of rechargeable lithium metal batteries [12–14]. Chemical shift NMR is particularly valuable for detecting dendritic structures, allowing us to distinguish between different electrochemical environments within the cell [11,15–17]. Moreover, the use of <sup>6</sup>Li and <sup>7</sup>Li isotopes in MRI facilitates the direct imaging of dendritic growth. <sup>7</sup>Li MRI, in particular, provides real-time visualization of dendritic formation [14,18–20]. Recently, indirect MRI was used in detecting the growth of dendrites based on their effects on the surrounding electrolyte [21]. The effects studied were displaced volume of the electrolyte, magnetic susceptibility effects on the electrolyte, and RF field effects on the electrolyte signal. As the electrolyte is typically composed of proton-rich material, the <sup>1</sup>H signal is much stronger compared to <sup>6</sup>Li and <sup>7</sup>Li MRI. This method allows for fast 3D MRI experiments with high resolution, providing a more comprehensive understanding of dendrite growth dynamics. In addition to imaging the evolution of the morphology of deposited lithium in a cell, MRI has also been used to characterize electrical currents within cells [22]. NMR and MRI techniques provide a multifaceted approach to understanding and mitigating dendritic growth in lithium batteries. Their integration of direct and indirect imaging methods, along with their capability to characterize internal currents, positions these techniques as indispensable tools in the quest for safer battery technologies.

This study focuses on the comparison of dendrite formation in batteries of different circuits of cells—a single cell, cells in parallel, and cells in series. Our hypothesis is that the growth of dendrites in series-connected cells is uniform and self-regulated, as the same current flows through each of these cells, while this is not the case for parallel-connected cells, where the current in the cells can be different and so is the growth of dendrites. This study was performed on the batteries of symmetrical Li-metal electrode cells that were sequentially imaged by 3D MRI during the charging process. The measured 3D images of the electrolyte in the cells were then analyzed to extract the morphological development of dendrites and to identify the effects of the circuit type on the growth patterns. This approach allows us to evaluate the dendrite growth mitigation performance for each type of circuit, which could facilitate the design of safer and more efficient lithium metal batteries.

## 2. Materials and Methods

### 2.1. Sample Preparation

The battery was assembled in one of three different configurations—as a single cell, cells in parallel, or cells in series—as shown in Figure 1. The battery body components were fabricated using stereolithography (SLA) 3D printing technology using a Prusa SL1S printer with Prusament Tough resin (Prusa Research, Prague, Czech Republic). For the electrodes, two square 0.3 mm thick lithium metal plates were stamped from a roll of lithium foil. The electrolyte was a solution of 1 M LiPF<sub>6</sub> in a volumetric mixture of ethylene carbonate (EC) and dimethyl carbonate (DMC) in a 1:1 ratio. Strips of copper foil were used as current collectors. These strips were stretched through specific slots in the cell housing and then sealed. The lithium electrodes were inserted into the corresponding slots of the housing during the assembly of the battery. This was then filled with electrolyte and sealed with a screw top. Battery assembly was performed in an argon-filled glove box (Vigor Gas Purification Technologies, Marktheidenfeld, Germany). Before inserting the battery into the MRI magnet, it was connected to a constant current source.

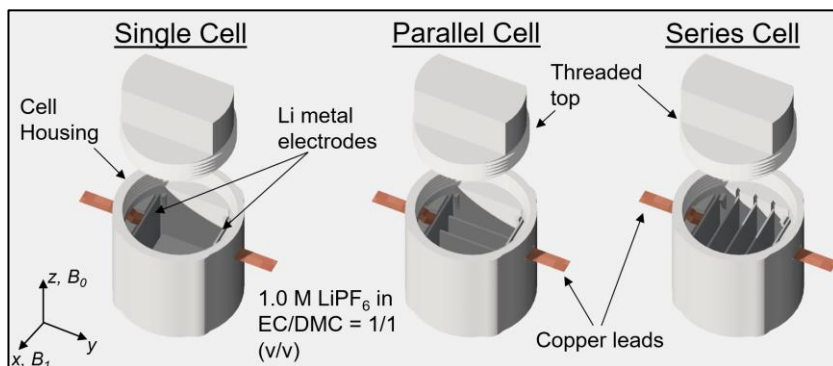


**Figure 1.** Cell assembly and its orientation in the MRI magnet relative to  $B_0$  and  $B_1$ .

## 2.2. Magnetic Resonance Imaging

The MRI experiments were performed using a 9.4 T (400 MHz proton frequency) wide-bore vertical magnet (Jastec, Tokyo, Japan) equipped with a Bruker Micro 2.5 gradient system (Bruker, Ettlingen, Germany), which was controlled by a Tecmag Redstone spectrometer (Tecmag, Houston, TX, USA). Data acquisition was performed with a 30 mm quadrature Bruker RF probe operating in linear polarization mode.

For optimal imaging, the cell was aligned inside the magnet so that the  $B_0$  and  $B_1$  magnetic fields were parallel to the electrode faces. We performed 3D  $^1\text{H}$  MRI using a 3D RARE sequence with the following parameters: inter-TE of 5.8 ms, TR of 2030 ms, and ETL of 8. The field of view was set to  $24 \times 24 \times 12$  mm across the  $x$ ,  $y$ , and  $z$  axes, with a  $128 \times 128 \times 64$  signal acquisition matrix in the following directions: read ( $x$ ), first phase ( $y$ ), and second phase ( $z$ ). This setup yielded a 3D image that encompassed both electrodes and the electrolyte region, with an isotropic resolution of  $187.5 \mu\text{m}$ .

Dendrite growth began concurrently with the start of  $^1\text{H}$  MRI image acquisition, maintaining a constant charging current of 1 mA throughout the experiment, with an upper voltage limit of 4.0 V. Each image acquisition lasted approximately 2 h and 20 min, followed by a 1 h pause before starting the next image acquisition. In total, for each battery configuration (single cell, cells in parallel, cells in series), 20 sequential images were acquired, which corresponded to 67 h of experiment time.

## 2.3. Image Analysis

The first step in the image analysis was to determine an intensity threshold indicating the boundary between dendritic and pure electrolyte voxels. This was performed through image histogram analysis, which involved calculating the histograms of all images in the sequence, followed by subtracting the histogram of the base (first) image from these. These ‘difference histograms’ were analyzed to identify a transition point—where the number of low-intensity voxels increased and high-intensity voxels decreased—which represented the threshold intensity. After determining the threshold intensity for each image, inverted thresholding was performed, where voxels with values below the threshold were assigned a value of 1, and other voxels were assigned a value of 0. These masks were then manually corrected for the possible inclusion of artifacts due to gas bubbles or other image imperfections.

Further analysis was focused on extracting the apparent and more accurate dendrite volume as a function of battery charge time. The apparent volume of dendritic structures  $V_{\text{apparent}}$  was simply equal to the sum of all dendritic voxel volumes, i.e., voxels with an intensity of 1 in the inverted-threshold MR images. As this results in an overestimation of the amount of lithium transferred between the electrodes during charging, this estimate must be further calibrated. In this study, this was achieved using a simple model in which all dendritic voxels were assumed to contain the same volumetric fraction  $f$  of lithium at a given charging time. This fraction was then determined by equating the product  $f \cdot \sum V_{\text{apparent}}$ , where the sum includes all cells of all battery configurations, with the

corresponding sum of the dendritic volume transferred between the electrodes according to the laws of electrolysis in all cells of all battery configurations  $\sum V_{\text{electrolysis}}$ . From here follows

$$f = \frac{\sum V_{\text{electrolysis}}}{\sum V_{\text{apparent}}}. \quad (1)$$

Note that the  $f$ -factor thus determined is calibrated for each time point and, in principle, can change with charging time. Knowing the  $f$ -factor makes it possible to estimate the amount of lithium transferred between electrodes for any cell of any battery configuration.

$$V_{\text{dendrite}} = f \cdot V_{\text{apparent}}. \quad (2)$$

### 3. Results

Figure 2 (Columns A, C, E) displays sequential 3D MR images of dendritic growth in symmetrical lithium metal electrode cells over time. The growth was due to a constant total current of 1 mA through the circuit and was the same in the three cases studied. These images show a representative slice ( $xy$  plane) through the cells, which best displays the morphology of the dendrite structure development across the cells. In the MR images, the electrolyte is bright, while the dendrites correspond to signal voids. In the case of a parallel circuit of cells (Column C), dendritic growth patterns are observed within the compartments formed by the dividing walls. The third cell shows notably less dendrite development compared to the other cells. In the case of a series circuit of cells (Column E), dendritic formations appear more uniform across the cells, with cells 1 and 2 showing initial rapid growth. Gas pockets are visible as dark circles on the MR images and can thus be easily distinguished from dendrites, which have more irregular shapes. The presence of gas pockets and their sizes vary according to the different types of circuits. In a parallel circuit, these pockets remain small and are confined within individual compartments. The signal intensity variation in the vicinity of the metal electrodes, which is best seen in the single cell and in parallel cells, is mostly due to the eddy currents induced by the  $B_1$  field and the susceptibility effects of the  $B_0$  field. These effects were already minimized by properly orienting the battery cells in the MRI magnet, as described in [23,24], but their complete elimination is not practically possible.

In order to optimally determine the image threshold required for the segmentation of dendritic structures from MR images, the temporal evolution of the image intensity distribution was also analyzed. For the single-cell experiment, this analysis is shown in Figure 3A, with an image of stacked histograms in which each color-coded row corresponds to an image histogram at a given time point, i.e., the row corresponds to the time point and the column to the bin index (image intensity), while the brightness (color) corresponds to the voxel count of the bin. From this image, it can be seen that the image histograms at the beginning ( $t < 20$  h) have one dominant line around a voxel intensity of 100, corresponding to electrolyte-rich regions, and one emerging line around an intensity of 10, corresponding to the deposited lithium on the anode. This line becomes much more intense with time, which can be explained by the increasing amount of deposited lithium. In addition to this dominant line, two significantly weaker lines appear around intensities of 70 and 120. These two lines later merge into one broader line that reaches an intensity of 220 and narrows to an intensity of 180 after  $t = 40$  h. The image threshold was then determined from the difference between the current and baseline (first) image histograms as the transition point (intensity) between intervals of increasing and decreasing voxel counts. For the histograms in Figure 3A, this analysis is shown in Figure 3B with a color-coded image of stacked histogram differences in rows. This image has two distinct regions, one with an increasing voxel count (in red) and the other with a decreasing voxel count (in blue), that are separated by a transition region with a stationary voxel count at an intensity of about 50, corresponding to the threshold. Note that the transition between these two regions is less clear with the first few images, as there is little change in the development of the image then.

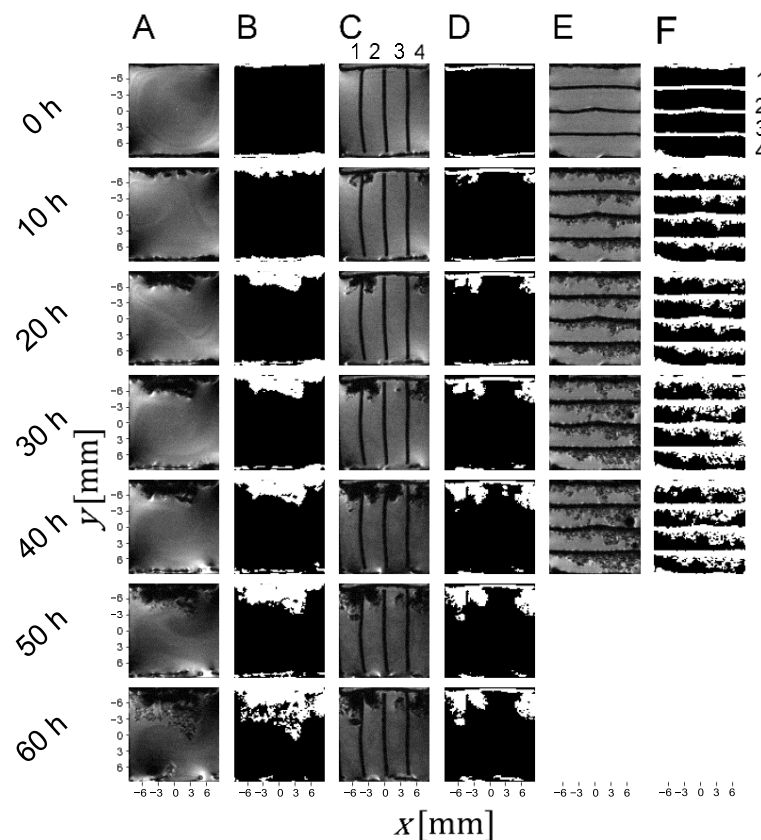


**Figure 2.** Columns (A,C,E) depict MRI scans of a single electrolytic cell and of electrolytic cells connected in parallel and in series, respectively, capturing dendritic growth over time. Columns (B,D,F) present the corresponding inverted threshold images, highlighting the dendrites and electrodes against the cell background for clarity. The numbers (1–4) next to cells in parallel and cells in series indicate cell indices.

Once the optimal thresholds were determined for each MR image of the experiment, the dendritic structures were segmented using inverted thresholding (Figure 2, columns B, D, F), in which dendrites and electrodes were assigned a binary value of 1, and the rest of the image was assigned a binary value of 0. This allowed for the quantification of the apparent dendrite volume, which was calculated as the sum of the volumes of all dendritic voxels (binary value 1) of all slices in the region between the electrodes. The graphs in Figure 4 show the resulting apparent dendrite volumes ( $V_{apparent}$ ) per electrode surface area ( $S_{electrode}$ ) as a function of time for cells connected in parallel (panel A) and for cells connected in series (panel B). For reference, each graph also contains this dependence for a single-cell experiment (blue circles). The plot of the growth for a single cell shows a deviation from linear growth, representing a sigmoidal trend, with a steep rate of growth in the first 19 h, then slowing down and increasing again around the 40th hour of measurement. The plots of dendrite growth for cells in parallel show different rates of growth, with cell number 3 showing a minimal increase. A plot of the average growth of cells in parallel (red triangles) shows the growth with the best linearity. In this case, the growth is similar to that in the single-cell experiment. The plots of dendrite growth for cells in series are more similar to each other and also to the plots for growth in the single-cell experiment. The exception is cell number 4, which shows a rapid initial growth rate that later approaches the growth rates of the other cells. As expected, the growth uniformity is much greater for cells in series than for cells in parallel. Note that in the series cell configuration, dendrites start to reach the opposite electrode after about 28 h. For this reason, the experimental points for cells in series do not exist after this time point. The dashed line in the graphs

corresponding to the linear growth model is derived from Faraday's law of electrolysis for a constant charging current of 1 mA.

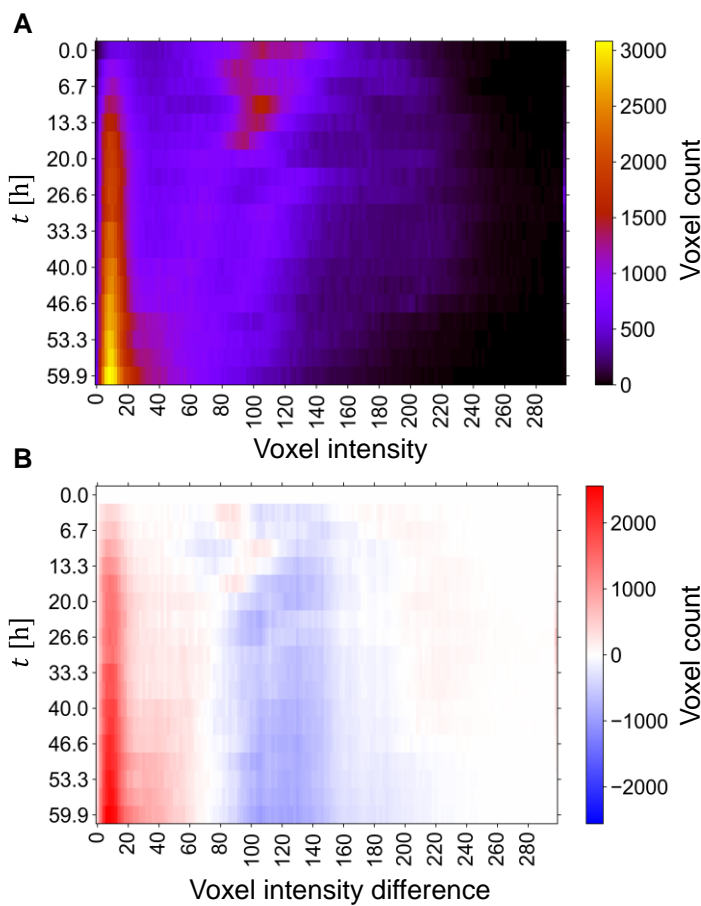


**Figure 3.** Temporal stack of (A) image intensity histograms and (B) differences between the current and baseline image intensity histograms. The histogram (or its difference) at a given time point is presented as a color-coded row. (A) The histogram stack image highlights the transition from the initial electrolyte dominance to subsequent dendritic growth, (B) while the stacked image of the corresponding histogram differences from the baseline allows for the determination of the image threshold for the segmentation of dendritic structures as a transition point between intervals of increasing and decreasing voxel counts.

Figure 5 shows the development of the anode plating in a representative slice across a single cell with images taken at 20 h intervals. The images are a result of processing that involves subtraction of the current image from the baseline (first) image, followed by normalization of this result to the average intensity of the electrolyte and final multiplication with a mask created by the inverted thresholding (Figure 2). This results in an image with an intensity of 0 in the electrolyte region and intensities from the threshold to 1 in the dendritic voxels. Here, an intensity of 1 (white voxel) indicates that a significant part of the voxel is filled with dendrites, so in this voxel, no MR signal was produced due to the physical presence of the dendrite or its influence on the magnetic fields around it and, thus, disturbed signal reception. A dendritic voxel with an intensity of less than 1 (gray voxel) filled with fewer dendrites. Apparently, there is a positive correlation between the intensity of a dendritic voxel and the proportion of dendrites in it, but a more precise relation between the two is difficult to find without a theoretical analysis of the MR signal around electrically conductive structures of the dendritic shape [21].

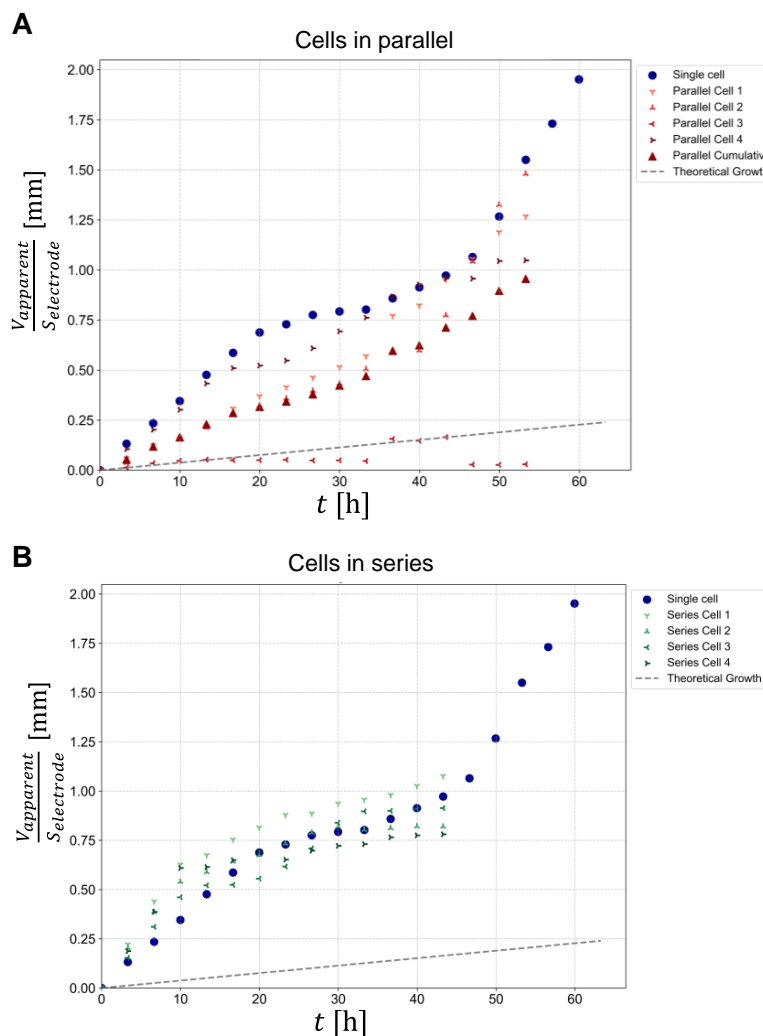


**Figure 4.** Graphs of the apparent dendrite volume (volume of all dendritic voxels) per electrode surface area as a function of charging time for (A) cells in parallel and (B) cells in series. Dendritic voxels were determined by inverted thresholding, as shown in the examples in Figure 2. The graphs also include plots of growth for a single cell (blue circles) and an average cell (red triangles, for cells in parallel only). The dashed line shows the theoretically expected volume of the deposited lithium per electrode surface area as a function of time.

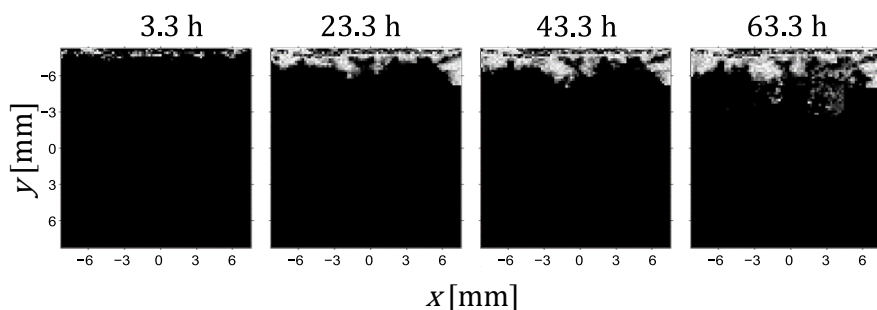


**Figure 5.** Time-lapse of images of a slice across a single cell at 3.3, 23.3, 43.3, and 63.3 h. The images are a result of processing that involves subtraction of the current image from the baseline image, normalization to the average intensity of the electrolyte, and multiplication with a mask created by the inverted thresholding (Figure 2). The images illustrate the progressive development of dendritic structures within the cell. A lighter shade of gray in dendritic voxels corresponds to a larger proportion of the voxel filled with dendrites.

A comparison between the  $V_{\text{apparent}} / S_{\text{electrode}}$  plots (different symbols) and the theoretically predicted volume of deposited lithium per electrode surface area (dashed line) in the graphs of Figure 4 shows that the latter is significantly smaller for any cell of any battery configuration. This discrepancy is due to dendritic voxels being only partially filled with lithium. We propose a simple solution to this discrepancy, namely a correction based on the assumption that all dendritic voxels are filled with lithium with the same fraction  $f$ . This  $f$ -fraction was determined for each time point as the ratio between the deposited lithium per electrode area according to the theory divided by the average of  $V_{\text{apparent}} / S_{\text{electrode}}$  over all cells in all experiments (Equation (1)). With a known value of  $f$ , the apparent volume of dendritic structures  $V_{\text{apparent}}$  can be replaced by a more precise measure for the volume of dendrites  $V_{\text{dendrite}}$  equal to  $f \cdot V_{\text{apparent}}$ . With this correction/calibration, the plots of  $V_{\text{apparent}} / S_{\text{electrode}}$  from Figure 4 transform into their calibrated equivalents of  $V_{\text{dendrite}} / S_{\text{electrode}}$  as a function of time for all cells and battery configurations that are shown in Figure 6. From these plots, it can be seen that on average, these values are close to the theoretical values for the volume of deposited lithium per electrode surface area. In addition, it can be clearly seen that the plots of  $V_{\text{dendrite}} / S_{\text{electrode}}$  are much more uniform for different cells in the case of cells in series (panel B) than in the case of cells in parallel (panel A).

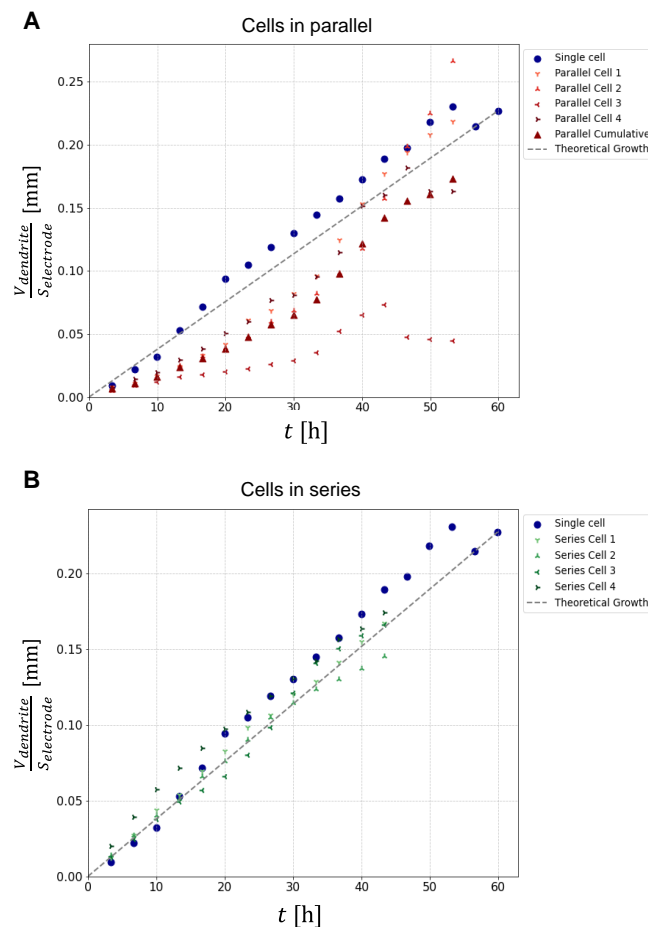


**Figure 6.** Graphs of the dendrite volume (deposited lithium on the anode) per electrode surface area as a function of charging time for (A) cells in parallel and (B) cells in series. The volumes of dendritic voxels  $V_{\text{apparent}}$  from Figure 4 were multiplied by the lithium filling fraction  $f$  to perform an assessment of the deposited lithium  $V_{\text{dendrite}}$ . The graphs also include plots of growth for a single cell (blue circles) and an average cell (red triangles, for cells in parallel only). The dashed line shows the theoretically expected volume of the deposited lithium per electrode surface area as a function of time.

The graph in Figure 7 depicts the dependencies of the  $f$ -factor and the signal  $S$  against charging time  $t$ . The signal  $S$  corresponds to an average MR signal of dendritic voxels normalized to the signal of the electrolyte. From the graph, it can be seen that the voxels with a lower filling factor  $f$  produce a higher signal  $S$ , and are found mostly at the beginning of the experiment, while the voxels with a higher filling factor  $f$  produce a lower signal  $S$ , and occur mostly in the second half of the experiment. It can also be seen that both the  $f$ -factor plot and the signal  $S$  plot flatten after  $t = 40$  h.

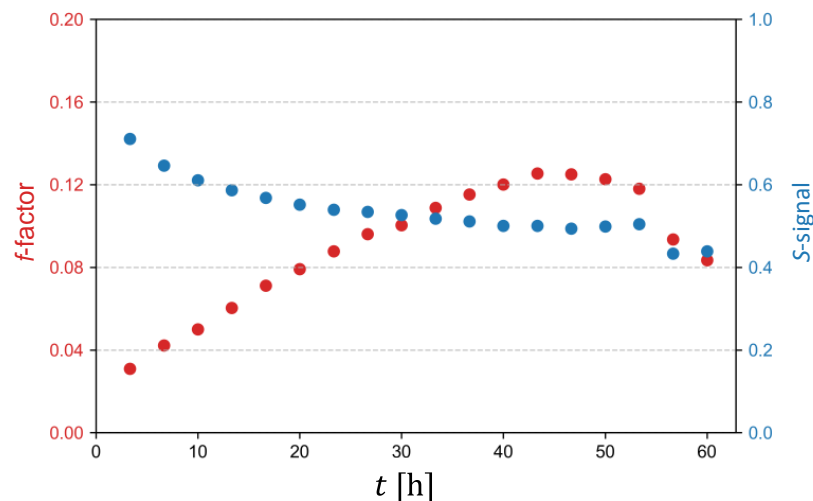


**Figure 7.** Graph of dendritic voxel filling factor with lithium  $f$  and of average MR signal of dendritic voxels normalized to the MR signal of electrolyte  $S$  as a function of charging time  $t$ .

#### 4. Discussion

$^1\text{H}$  MR imaging of the electrolyte region enabled the indirect detection of dendritic structures in the images in the form of dark, branched shapes on the anodes of symmetric lithium cells (Figure 2A,C,E). As can be best seen from the images of a single cell (Figure 2A), initially, the deposits are dense and moss-like, but in the later stages of the experiment, they develop a more branched structure. This is also seen to some extent in the parallel cell experiment (Figure 2C), but interestingly, not so much in the series cell configuration (Figure 2E). This may be a result of the development of the lithium salt concentration profile in the electrolyte, which, in turn, dictates the start time of dendritic growth, as per the Sand's model [10]. As the distance between the electrodes shortens with time, the concentration gradient established with time is steeper, which may explain the greater branching of the latter structures. Dendrites tend to grow towards regions of higher ion concentration, as these regions provide more material for deposition [10,25]. A steeper concentration gradient can thus cause more pronounced and faster growth of dendrites. Another reason for their faster growth could be the increase in the electric field in regions with smaller interelectrode distances. For example, Chazalviel's model states that the growth rate of dendrites is proportional to the factor of anion mobility and the electric field ( $v = -\mu_a E$ ) [10]. The distinct transition between the dense and branched morphologies can be explained by the fact that high current densities lead to inhomogeneous lithium-ion flux at the electrode–electrolyte interface, leading to uneven lithium deposition and the formation of dendritic structures. At lower current densities, lithium ions have sufficient time to diffuse evenly across the electrode surface, promoting the formation of a smooth, dense lithium layer. However, as current density increases, the rate of lithium-ion deposition surpasses the diffusion rate, resulting in localized areas of high lithium-ion concentration and subsequent dendritic growth. Furthermore, the concentration gradient of lithium ions in the electrolyte is a dynamic factor during battery operation. As lithium ions are plated onto the anode during charging, their concentration near the electrode surface decreases, potentially

leading to uneven deposition if the ions in the electrolyte at the anode are not replenished quickly enough [26].

The assessment of the development of dendritic growth in cells in series configuration reveals remarkable uniformity in growth rates. In a representative MRI slice, the volume of dendrites is approximately equal in all cells at each time point, with all dendritic structures reaching the opposite electrode at approximately the same time (after approximately 28 h). This suggests the existence of some kind of self-regulatory mechanism in which the existence of a runaway cell is unlikely. In this configuration, the current through all the cells is the same, and so is the dendrite growth rate, which means that the amount of lithium deposited must be the same in all cells at all times. Note that this can still not explain the uniformity of dendrite growth across the anode surface, as this is still a very uncontrollable phenomenon.

In the case of parallel cell configuration, all four separate cells are connected to the same source and thus have the same electric potential. This basically means that if there is a cell with a faster dendrite growth rate, that cell has relatively lower resistance than the rest of the cells and, thus, a proportionally higher current. This further accelerates the growth of dendrites in this cell compared to the rest of the cells, resulting in a runaway cell. Another factor that indicates that this configuration is disadvantageous compared to the single cell is the fact that ion diffusion is limited from the neighboring cell, which means that in theory, local concentration gradients should be much higher in cases where cells are narrower. Note that in our experiments, the cells were not completely isolated from each other; therefore, some amount of lateral ion diffusion is still permitted in the vicinity of electrodes.

Numerous studies have focused on the morphology of dendritic structures and found their typical scale to be in the range of 1–3  $\mu\text{m}$  [27]. In contrast, the voxel size used in our experiments was 187  $\mu\text{m}$ . However, this limitation of MRI resolution is not the only confining factor; signal attenuation due to magnetic susceptibility and RF shielding effects are also very important. The extent of this attenuation depends not only on the dendrite volume-to-voxel volume ratio, but also on the shape and orientation of the dendrite with respect to the magnetic fields  $B_0$  and  $B_1$  [21,24]. As a result, images generated by the indirect imaging technique have limitations in providing direct information about the specific properties of dendrites, such as their density. The graphs of the apparent dendrite volume per electrode area as a function of charging time in Figure 4 offer several interesting insights. First, we can see that the apparent dendrite volume is up to ten times larger than the corresponding theoretical value of deposited lithium per electrode area, which is about 0.25  $\text{mm}^3$  per 1  $\text{mm}^2$  of the electrode after 60 h. Second, contrary to theoretical expectations, the growth of apparent dendritic volume is non-linear. This growth pattern indicates the presence of different growth regimes at different charging times, resulting in dendrites of different structures and, thus, different effects on MR signal reduction. Thus, the growth of the apparent dendrite volume is gradual in denser dendrites, while it is faster in more branched dendritic structures. There is also a marked difference in the dendrite volume growth among different battery configurations. Specifically, in the parallel cell configuration the growth is significantly more pronounced compared to the series cell configuration. This finding highlights the importance of cell configuration in influencing dendrite growth patterns in lithium-ion batteries.

The presence of gas pockets in all configurations and their random changes raise questions about chemical reactions or possible leaks in the battery case. The composition of the electrolyte must be stable in the operating voltage and temperature ranges [28]. Although moisture levels were consistently below 1 ppm during assembly, LiPF<sub>6</sub> is sensitive to traces of moisture present in the electrolyte and will react with these impurities to produce a small amount of hydrofluoric acid (HF) [29]. It could also be that the sealing of the assembled cell was compromised, allowing moisture from the environment to enter the cell during the experiments. As for the effect of the formation of gas bubbles, they will disturb the dendrite formation process by disrupting the flow of the electric current. Given the

sensitive nature of lithium dendrites, it is likely that forces arising from surface tension may also influence the development and morphology of these dendritic structures. However, this phenomenon requires further investigation to develop a better understanding.

In the original publication on indirect lithium dendrite imaging [21], the authors used a FLASH imaging sequence to calculate the dendrite volume fraction from the image signal intensity. Given that FLASH is a gradient-echo sequence, it is more sensitive to  $B_0$  inhomogeneities and thus to susceptibility effects, which were identified in this study as major contributors to signal attenuation. However, a different MRI sequence was used in this study, namely the RARE imaging sequence, which is based on spin-echo and is therefore less susceptible to magnetic susceptibility effects and thus to dendritic structures than the FLASH sequence. The sensitivity of the used imaging sequence to magnetic susceptibility and to RF shielding may affect the threshold settings for the correct segmentation of dendrites or the ratio of the MR signal to the dendrite volume fraction. The direct determination of lithium volume fraction from the normalized MR signal remains a possible better alternative to thresholding for our future studies. One such relation can already be discerned from Figure 7 of this study, i.e., the relation between the  $f$ -factor (lithium volume fraction) and the normalized signal  $S$ . However, this relation only applies to the mean values of dendritic voxels, and not to all voxels and all of their values at any given time in the experiment. For example, at the beginning of the experiment, dendrites are less developed and less dense, while later in the experiment, they are more developed and therefore denser. Due to the different structures of dendrites, their effect on reducing the MR signal is different, i.e., a lower amount of lithium in earlier dendrites can cause the same reduction in the MR signal as a higher amount of lithium in later dendrites.

## 5. Conclusions

In this study, an indirect imaging approach based on  $^1\text{H}$  MRI of an electrolyte was used to monitor dendritic growth in three different configurations of lithium symmetric cells: single cell, cells in series, and cells in parallel. A volumetric analysis of dendritic growth on the measured sequential images confirmed the expectation that growth is most uniform in the series cell configuration, while it is compromised by the likely possibility of a runaway cell ending in a short circuit in the parallel configuration. A comparison between the volume of all dendritic voxels and the volume of transferred lithium according to the laws of electrolysis showed that dendritic voxels are only partially filled with lithium. In this study, the filling fraction was determined based on this comparison. In future studies, after appropriate calibration, this fraction could be determined directly from the voxel signal.

**Author Contributions:** Conceptualization, R.P., U.M. and I.S.; methodology, R.P. and U.M.; software, R.P.; formal analysis, R.P.; investigation, R.P., U.M. and I.S.; resources, I.S.; writing—original draft preparation, R.P., U.M. and I.S.; supervision, I.S. All authors have read and agreed to the published version of the manuscript.

**Funding:** This research was funded by the Slovenian Research and Innovation Agency grant P1-0060, “Experimental biophysics of complex systems and imaging in biomedicine”.

**Data Availability Statement:** The data presented in this study are available on request from the corresponding author.

**Acknowledgments:** The authors thank Ana Sepe for providing technical support and Megha Manikandan for proofreading the manuscript.

**Conflicts of Interest:** The authors declare no conflicts of interest.

## References

1. Tarascon, J.M.; Armand, M. Issues and challenges facing rechargeable lithium batteries. *Nature* **2001**, *414*, 359–367. [[CrossRef](#)] [[PubMed](#)]
2. Jana, A.; Woo, S.I.; Vikrant, K.S.N.; García, R.E. Electrochemomechanics of lithium dendrite growth. *Energy Environ. Sci.* **2019**, *12*, 3595–3607. [[CrossRef](#)]
3. Bai, P.; Li, J.; Brushett, F.R.; Bazant, M.Z. Transition of lithium growth mechanisms in liquid electrolytes. *Energy Environ. Sci.* **2016**, *9*, 3221–3229. [[CrossRef](#)]
4. Ma, Y.; Wu, F.; Chen, N.; Ma, Y.T.; Yang, C.; Shang, Y.X.; Liu, H.X.; Li, L.; Chen, R.J. Reversing the dendrite growth direction and eliminating the concentration polarization an internal electric field for stable lithium metal anodes. *Chem. Sci.* **2022**, *13*, 9277–9284. [[CrossRef](#)] [[PubMed](#)]
5. He, L.C.; Sun, Q.M.; Lu, L.; Adams, S. Understanding and Preventing Dendrite Growth in Lithium Metal Batteries. *Accts Appl. Mater. Inter.* **2021**, *13*, 34320–34331. [[CrossRef](#)] [[PubMed](#)]
6. Li, Y.J.; Jiao, J.Y.; Bi, J.P.; Wang, X.F.; Wang, Z.X.; Chen, L.Q. Controlled deposition of Li metal. *Nano Energy* **2017**, *32*, 241–246. [[CrossRef](#)]
7. Park, J.; Jeong, J.; Lee, Y.; Oh, M.; Ryou, M.H.; Lee, Y.M. Micro-Patterned Lithium Metal Anodes with Suppressed Dendrite Formation for Post Lithium-Ion Batteries. *Adv. Mater. Interfaces* **2016**, *3*, 1600140. [[CrossRef](#)]
8. Park, J.; Kim, D.; Jin, D.; Phatak, C.; Cho, K.Y.; Lee, Y.G.; Hong, S.; Ryou, M.H.; Lee, Y.M. Size effects of micro-pattern on lithium metal surface on the electrochemical performance of lithium metal secondary batteries. *J. Power Sources* **2018**, *408*, 136–142. [[CrossRef](#)]
9. Ryou, M.H.; Lee, Y.M.; Lee, Y.J.; Winter, M.; Bieker, P. Mechanical Surface Modification of Lithium Metal: Towards Improved Li Metal Anode Performance by Directed Li Plating. *Adv. Funct. Mater.* **2015**, *25*, 834–841. [[CrossRef](#)]
10. Shen, L.; Shi, P.R.; Hao, X.G.; Zhao, Q.; Ma, J.B.; He, Y.B.; Kang, F.Y. Progress on Lithium Dendrite Suppression Strategies from the Interior to Exterior by Hierarchical Structure Designs. *Small* **2020**, *16*, e2000699. [[CrossRef](#)]
11. Hu, J.Z.; Zhao, Z.C.; Hu, M.Y.; Feng, J.; Deng, X.C.; Chen, X.L.; Xu, W.; Liu, J.; Zhang, J.G. In situ <sup>7</sup>Li and <sup>133</sup>Cs nuclear magnetic resonance investigations on the role of Cs<sup>+</sup> additive in lithium-metal deposition process. *J. Power Sources* **2016**, *304*, 51–59. [[CrossRef](#)]
12. Liu, D.Q.; Shadike, Z.; Lin, R.Q.; Qian, K.; Li, H.; Li, K.K.; Wang, S.W.; Yu, Q.P.; Liu, M.; Ganapathy, S.; et al. Review of Recent Development of In Situ/Operando Characterization Techniques for Lithium Battery Research. *Adv. Mater.* **2019**, *31*, e1806620. [[CrossRef](#)] [[PubMed](#)]
13. Eastwood, D.S.; Bayley, P.M.; Chang, H.J.; Taiwo, O.O.; Vila-Comamala, J.; Brett, D.J.L.; Rau, C.; Withers, P.J.; Shearing, P.R.; Grey, C.P.; et al. Three-dimensional characterization of electrodeposited lithium microstructures using synchrotron X-ray phase contrast imaging. *Chem. Commun.* **2015**, *51*, 266–268. [[CrossRef](#)] [[PubMed](#)]
14. Foroozan, T.; Sharifi-Asl, S.; Shahbazian-Yassar, R. Mechanistic understanding of Li dendrites growth by imaging techniques. *J. Power Sources* **2020**, *461*, 228135. [[CrossRef](#)]
15. Bhattacharyya, R.; Key, B.; Chen, H.L.; Best, A.S.; Hollenkamp, A.F.; Grey, C.P. NMR observation of the formation of metallic lithium microstructures in lithium batteries. *Nat. Mater.* **2010**, *9*, 504–510. [[CrossRef](#)] [[PubMed](#)]
16. Chang, H.J.; Trease, N.M.; Ilott, A.J.; Zeng, D.L.; Du, L.S.; Jerschow, A.; Grey, C.P. Investigating Li Microstructure Formation on Li Anodes for Lithium Batteries by in Situ <sup>6</sup>Li/<sup>7</sup>Li NMR and SEM. *J. Phys. Chem. C* **2015**, *119*, 16443–16451. [[CrossRef](#)]
17. Gunnarsdóttir, A.B.; Amanchukwu, C.V.; Menkin, S.; Grey, C.P. Noninvasive NMR Study of “Dead Lithium” Formation and Lithium Corrosion in Full-Cell Lithium Metal Batteries. *J. Am. Chem. Soc.* **2020**, *142*, 20814–20827. [[CrossRef](#)] [[PubMed](#)]
18. Chandrashekhar, S.; Trease, N.M.; Chang, H.J.; Du, L.S.; Grey, C.P.; Jerschow, A. <sup>7</sup>Li MRI of Li batteries reveals location of microstructural lithium. *Nat. Mater.* **2012**, *11*, 311–315. [[CrossRef](#)]
19. Chang, H.J.; Ilott, A.J.; Trease, N.M.; Mohammadi, M.; Jerschow, A.; Grey, C.P. Correlating Microstructural Lithium Metal Growth with Electrolyte Salt Depletion in Lithium Batteries Using Li MRI. *J. Am. Chem. Soc.* **2015**, *137*, 15209–15216. [[CrossRef](#)]
20. Ilott, A.J.; Chandrashekhar, S.; Kloeckner, A.; Chang, H.J.; Trease, N.M.; Grey, C.P.; Greengard, L.; Jerschow, A. Visualizing skin effects in conductors with MRI: <sup>7</sup>Li MRI experiments and calculations. *J. Magn. Reson.* **2014**, *245*, 143–149. [[CrossRef](#)]
21. Ilott, A.J.; Mohammadi, M.; Chang, H.J.; Grey, C.P.; Jerschow, A. Real-time 3D imaging of microstructure growth in battery cells using indirect MRI. *Proc. Natl. Acad. Sci. USA* **2016**, *113*, 10779–10784. [[CrossRef](#)]
22. Mohammadi, M.; Silletta, E.V.; Ilott, A.J.; Jerschow, A. Diagnosing current distributions in batteries with magnetic resonance imaging. *J. Magn. Reson.* **2019**, *309*, 106601. [[CrossRef](#)] [[PubMed](#)]
23. Britton, M.M. Magnetic Resonance Imaging of Electrochemical Cells Containing Bulk Metal. *Chemphyschem* **2014**, *15*, 1731–1736. [[CrossRef](#)]
24. Sersa, I.; Mikac, U. A study of MR signal reception from a model for a battery cell. *J. Magn. Reson.* **2018**, *294*, 7–15. [[CrossRef](#)]
25. Brissot, C.; Rosso, M.; Chazalviel, J.N.; Lascaud, S. In situ concentration cartography in the neighborhood of dendrites growing in lithium/polymer-electrolyte/lithium cells. *J. Electrochem. Soc.* **1999**, *146*, 4393–4400. [[CrossRef](#)]
26. Brissot, C.; Rosso, M.; Chazalviel, J.N.; Lascaud, S. Dendritic growth mechanisms in lithium/polymer cells. *J. Power Sources* **1999**, *81*, 925–929. [[CrossRef](#)]
27. Orsini, F.; Du Pasquier, A.; Beaudoin, B.; Tarascon, J.M.; Trentin, M.; Langenhuizen, N.; De Beer, E.; Notten, P. In situ Scanning Electron Microscopy (SEM) observation of interfaces within plastic lithium batteries. *J. Power Sources* **1998**, *76*, 19–29. [[CrossRef](#)]

28. Piglowska, M.; Kurc, B.; Galinski, M.; Fuc, P.; Kaminska, M.; Szymlet, N.; Daszkiewicz, P. Challenges for Safe Electrolytes Applied in Lithium-Ion Cells-A Review. *Materials* **2021**, *14*, 6783. [[CrossRef](#)]
29. Yang, Y.P.; Huang, A.C.; Tang, Y.; Liu, Y.C.; Wu, Z.H.; Zhou, H.L.; Li, Z.P.; Shu, C.M.; Jiang, J.C.; Xing, Z.X. Thermal Stability Analysis of Lithium-Ion Battery Electrolytes Based on Lithium Bis(trifluoromethanesulfonyl)imide-Lithium Difluoro(oxalato)Borate Dual-Salt. *Polymers* **2021**, *13*, 707. [[CrossRef](#)]

**Disclaimer/Publisher's Note:** The statements, opinions and data contained in all publications are solely those of the individual author(s) and contributor(s) and not of MDPI and/or the editor(s). MDPI and/or the editor(s) disclaim responsibility for any injury to people or property resulting from any ideas, methods, instructions or products referred to in the content.